Dalton Transactions

ROYAL SOCIETY OF CHEMISTRY

PAPER

View Article Online
View Journal | View Issue

Cite this: *Dalton Trans.*, 2024, **53**, 10142

Engineering hierarchical snowflake-like multi-metal selenide catalysts anchored on Ni foam for high-efficiency and stable overall water splitting†

Enze Fan,[a] Shuangqi Zhou,[a] Hanwei Zhao,[a] Jianxin Ran,[a] Zhuanfang Zhang,*[b] Guohua Dong,*[a] Wenzhi Zhang,[a] Yu Zang,[c] Ming Zhao,[a] Dong-Feng Chai[a] and Xiaoming Huang[b]

Received 15th April 2024,
Accepted 21st May 2024

DOI: 10.1039/d4dt01108b

rsc.li/dalton

The development of excellent bifunctional electrocatalysts is an effective way to promote the industrial application of electrolytic water. In this work, a free-standing W-doped cobalt selenide (W-CoSe300/NF) electrocatalyst with a snowflake-like structure supported on nickel foam was prepared by a hydrothermal–selenization strategy. Benefiting from the high specific surface area of the 3D snowflake-like structure and the regulation of tungsten doping on the electronic structure of the metal active center, W-CoSe300/NF shows remarkable electrocatalytic water decomposition performance. In 1.0 M KOH, the W-CoSe300/NF electrocatalyst achieved an efficient HER and OER at a current density of 50 mA cm^{-2} with overpotentials as low as 84 mV and 283 mV, respectively. More importantly, W-CoSe300/NF acts as both the anode and cathode of the electrolytic tank, requiring only a potential of 1.54 V to obtain 10 mA cm^{-2} and can operate continuously for more than 120 hours at this current density. This study proposes a new way for the design of high efficiency and affordable bifunctional electrocatalysts.

1. Introduction

With the accelerated consumption of unsustainable fossil fuels, electrocatalytic overall water splitting (OWS) has emerged as the most reliable route to prepare portable hydrogen fuel.[1–4] Moreover, the anodic oxygen evolution reaction (OER) is a complex process with multiple electron transfer reactions, a slow reaction rate and a high overpotential, which seriously hinders the development and industrial application of electrolytic water.[5,6] Noble metal-based materials (such as Pt, Ir, Ru, *etc.*) were once considered to be excellent catalytic materials for water electrolysis, but their low Earth abundance and high cost make them unable to be used in large-scale industrial applications.[7–9] Therefore, it is of excellent practical importance to develop efficient, cheap and Earth-abundant electrocatalysts to promote the industrialization process of electrocatalytic water decomposition.[10–12] For the past few years, a large number of inexpensive transition metal-based electrocatalysts have been designed, such as transition metal-based oxides, sulfides, selenides, nitrides, phosphates and carbides.[13,14] In particular, transition metal selenides exhibit excellent electrocatalytic activity in water electrolysis under alkaline conditions due to their outstanding electrical conductivity and antioxidant capacity.[15,16] However, the single component selenide material may still have insufficient active sites and poor stability, which will affect the actual electrocatalytic performance.[17,18] Therefore, it needs to be further modified to improve its electrocatalytic activity and stability.[19,20]

Metal element doping has been proved to optimize the energy band structure and active site density of electrocatalysts, thereby improving their electrocatalytic activity.[21–23] For example, Xin Yue *et al.* demonstrated that the addition of a few Mo heteroatoms (~0.5 wt%) to Co_3O_4 can enhance its activity and stability in the acidic OER.[24] This enhancement can be ascribed to the activation of lattice oxygen by the doping of Mo, leading to a well-defined etching process and oxygen vacancy generation. The obtained oxygen vacancies promote a rapid oxygen evolution reaction (OER) pathway, while the variable valence state of Mo contributes to its stability. Ji-Shuang Zeng *et al.* reported an $IrRuO_x$/C catalyst.[25] This study showed that the introduction of Ir can stabilize the lattice oxygen structure of RuO_x, enhance the Ru–O bond interaction, stabilize the solvation of Ru at high potentials, and accelerate the nucleophilic attack of water molecules, thus greatly improving the OER activity and durability. Liqing Wu

---

[a] *College of Chemical Engineering, Qiqihar University, Qiqihar 161006, PR China. E-mail: ghdong@qqhru.edu.cn*

[b] *Teaching Experiment Management Equipment Center, Qiqihar University, Qiqihar 161006, PR China. E-mail: zzfhao2014@163.com*

[c] *College of Materials, Qiqihar University, Qiqihar University, Qiqihar 161006, PR China*

† Electronic supplementary information (ESI) available. See DOI: **https://doi.org/10.1039/d4dt01108b**

et al. confirmed that Bi doping can effectively improve the initial valence state of metal Ru, which is the active center of the metal in $Bi_{0.15}Ru_{0.85}O_2$, thus improving the acidic OER kinetics of the catalyst.[26] Moreover, the interaction of electrons is significantly strengthened by the existence of bismuth by reducing the energy barrier, avoiding excessive oxidation of the active substance, maintaining the stability of the structure and improving the OER activity of the electrocatalyst. Yang Wang *et al.* reported a W-$NiS_{0.5}Se_{0.5}$ electrocatalyst with excellent HER and OER activities.[27] Theoretical calculations confirm that the increase in catalytic activity can be ascribed to the delocalization of the spin state of Ni by the introduction of a single atom W, resulting in an increase in the electron density of Ni, which optimizes the adsorption/desorption capacity of the H intermediate in the rate-determining step (O*-OOH*). Compared with other previously reported doping elements, tungsten (W) is an ideal dopant due to its ability to induce a phase transformation in the catalyst structure even at a very low doping content, resulting in improved catalytic activity and stability.[28] Based on the above considerations, the rational design of W-doped selenide electrocatalysts is of vital importance for the realization of efficient overall water decomposition.[29–31]

Herein, we prepared a W-doped cobalt selenide (W-CoSe300/NF) electrocatalyst and used it as a high-efficiency HER/OER dual functional electrocatalyst. The electrocatalytic water splitting experiments showed that W-CoSe300/NF could achieve efficient HER and OER processes at a current density of 50 mA cm^{-2} with overpotentials of 84 mV and 283 mV, respectively, in 1.0 M KOH. Furthermore, by using W-CoSe300/NF as both the cathode and anode of the cell for the overall electrolysis of water, the two-electrode system exhibits a fascinating electrolytic potential of 1.54 V and electrochemical durability of up to 120 hours. The outstanding electrocatalytic activity and stability of water decomposition shown by W-CoSe300/NF can be chiefly ascribed to the following four points: (i) cobalt selenide has significant electron transport capacity, which contributes to electron transfer during the electrocatalytic reaction, thus improving the efficiency of the electrocatalytic water decomposition. (ii) The doping of W adjusts the electronic environment of the metal, effectively increasing the number of catalytically active sites, thereby endowing the electrocatalyst with significant intrinsic activity. (iii) The 3D snowflake-like structure effectively increases the contact area between the electrode material and the electrolyte during the water decomposition reaction, so that more correct active sites are exposed. (iv) The free-standing structure of nickel foam effectively reduces the contact resistance between the electrocatalyst and the conductive substrate, which effectively promotes the activity and stability of W-CoSe300/NF.

2. Results and discussion

Materials, synthesis of the electrocatalyst, physical characterization, and electrochemical measurements in this study can be found in the ESI.†

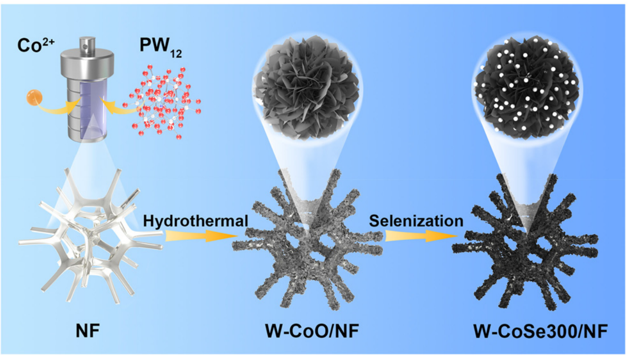

Fig. 1 Schematic diagram of the synthesis process of W-CoSe300/NF snowflake flakes.

The schematic diagram of the synthesis route of W-CoSe300/NF is shown in Fig. 1. The W-CoSe300 electrocatalyst was prepared by adding $H_3PW_{12}O_{40}$ and $C_4H_6CoO_4$ to NF under the conditions of hydrothermal and selenization heat treatment.

Scanning electron microscopy (SEM) is a technique to characterize the morphology and microstructure of the prepared catalysts. As seen in Fig. 2a, the W-CoO/NF precursor synthesized by a one-step hydrothermal reaction shows that the slices are cross-agglomerated to form snowflake flakes, and they are uniformly attached to the surface of nickel foam. Fig. 2b shows the SEM images of W-CoSe300/NF. The spherical morphology of the W-CoO/NF precursor is not damaged after high temperature selenization, and the snowflake flakes are evenly distributed on the sheets. Subsequently, transmission electron microscopy (TEM) is used to further affirm the snowflake-like structure of W-CoSe300/NF (Fig. 2c). In addition, it can be seen from Fig. S1† that W-CoSe300/NF synthesized at different selenization temperatures (200, 300 and 400 °C) all exhibit similar snowflake-like structures, with only differences in size. High-resolution transmission electron microscopy (HRTEM) images of W-CoSe300/NF are shown in Fig. 2d. It can be observed that the lattice spacing of 0.366 nm corresponds to the (220) plane of Co_9Se_8 (PDF#09-0223). Meanwhile, the lattice spacings of 0.316 nm and 0.321 nm observed in Fig. 2e can correspond to the (111) plane of Ni_3Se_2 (PDF#23-1227) and the (004) plane of WSe_2 (PDF#38-1338), respectively. It is worth noting that the appearance of W-CoSe300/NF can be attributed to the selenization of the nickel foam, which is consistent with previous reports.[32,33] Fig. 2f shows the selected area electron diffraction (SAED) pattern of W-CoSe300, in which the Co_9Se_8 (220), Ni_3Se_2 (111) and WSe_2 (004) planes can be observed, further confirming the analyses of HRTEM. Furthermore, the mapping images of energy dispersive X-ray spectroscopy (EDS) along with the corresponding table of elemental contents confirmed the coexistence of Co, Ni, Se, and W elements on the surface of the prepared catalyst samples (Fig. 2g and Fig. S2†). It is worth noting that trace amounts of O element can be observed in W-CoSe300/NF, which can be attributed to the partial oxidation of the surface of the catalyst after long-term

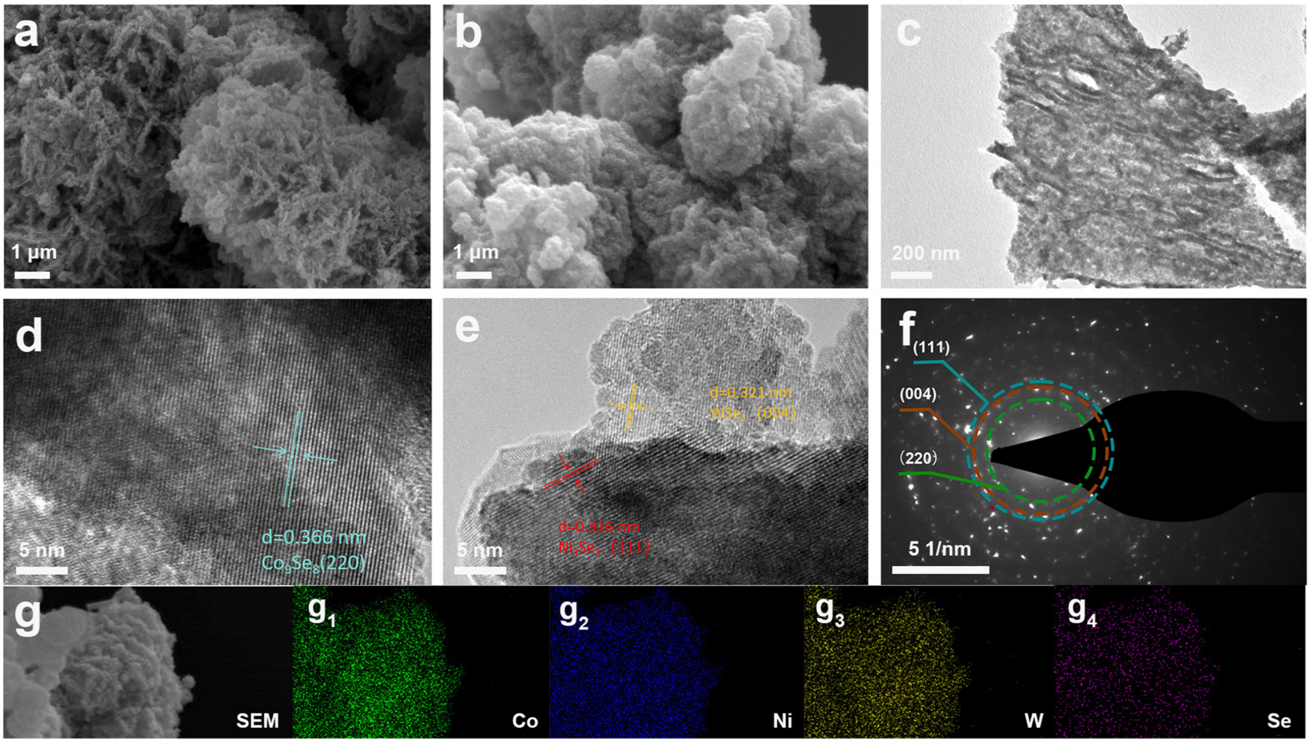

Fig. 2 (a) SEM images of the W-CoO/NF precursor. (b) SEM image, (c) TEM image, (d and e) HRTEM images, (f) SAED pattern, and (g) EDS elemental mapping images of W-CoSe300/NF.

exposure to air.[34] In short, the results of the above morphological analysis confirm the successful preparation of W-CoSe300/NF with a snowflake structure, which will facilitate the exposure of the active sites and thus promote the dissociation kinetics of water.

Fig. 3a shows the X-ray diffraction (XRD) pattern of W-CoSe300/NF. It can be clearly seen that the characteristic diffraction peaks at 27.37°, 29.27°, 45.45° and 49.86° correspond to the (111), (222), (511) and (440) planes of Co_9Se_8, respectively. The diffraction peaks at 29.37°, 32.42° and 45.66° correspond to the (111), (200) and (220) crystal faces of Ni_3Se_2, respectively, while the diffraction peaks at 32.73°, 38.30° and 70.03° correspond to the (101), (103) and (203) crystal faces of WSe_2, respectively. In the process of W-CoO/NF selenization, selenium replaced the O element to form a variety of transition metal polymetallic selenized complexes, thereby changing the original crystal structure and the electron transfer pathway, thus improving its electrochemical catalytic performance.[35]

In order to research the elemental composition and surface chemical states of samples, X-ray photoelectron spectroscopy (XPS) spectra were recorded, as described in Fig. 3b–f. According to Fig. 3b, the survey spectra of W-CoSe300/NF and W-CoO/NF show that the surface of W-CoSe300/NF is composed of Co, Ni, C, O, W and Se elements. Compared with the W-CoO/NF precursor, the Se element is added, which preliminarily proves the success of selenization of the precursor. From the XPS of high-resolution Co 2p, peaks at 803.68 eV and 785.18 eV in W-CoO/NF correspond to Sat, while the main peaks of binding energy of 797.38 eV and 781.38 eV are attributed to Co $2p_{1/2}$ and Co $2p_{3/2}$, respectively.[36–39] After selenization, the peak positions of W-CoSe300/NF are 802.68 eV and 785.08 eV and the peak positions of Co $2p_{1/2}$ and Co $2p_{3/2}$ are 796.68 eV and 780.68 eV (Fig. 3c). As shown in Fig. 3d, two peaks of W-CoO/NF at 874.48 eV and 856.58 eV correspond to Ni $2p_{1/2}$ and Ni $2p_{3/2}$, respectively.[40–42] The peak values of W-CoSe300/NF are 872.88 eV and 855.18 eV, respectively. This is also the same as the Se replaces the O, resulting in a negative peak shift. Fig. 3e shows the XPS spectrum of Se 3d. The characteristic peak at the position of 57.8 eV belongs to the Se–O peak, indicating that W-CoO/NF is not fully produced by selenization, and the characteristic peaks at the positions of 53.98 eV and 52.98 eV belong to Se $3d_{3/2}$ and Se $3d_{5/2}$, respectively.[43–45] Fig. 3f shows the characteristic peaks of W 4f for W-CoSe300/NF and W-CoO/NF. The peaks of W-CoO/NF at 37.68 eV and 35.48 eV correspond to W $4f_{5/2}$ and W $4f_{7/2}$, respectively.[46–48] The corresponding peak values of W-CoSe300/NF are 37.08 eV and 34.98 eV, respectively. The peak value also shifted negatively with an average value of 0.55 eV.

A standard three-electrode system of 1.0 M KOH was used to assess the HER performance of all the electrocatalysts. Firstly, a series of pre-tests were performed to explore the material and solution ratio, reaction temperature and time required for the reaction, and the optimal preparation conditions of the precursors were determined, as illustrated in Fig. S3–S6.† Subsequently, the HER properties of the catalyst samples obtained under different selenization conditions were

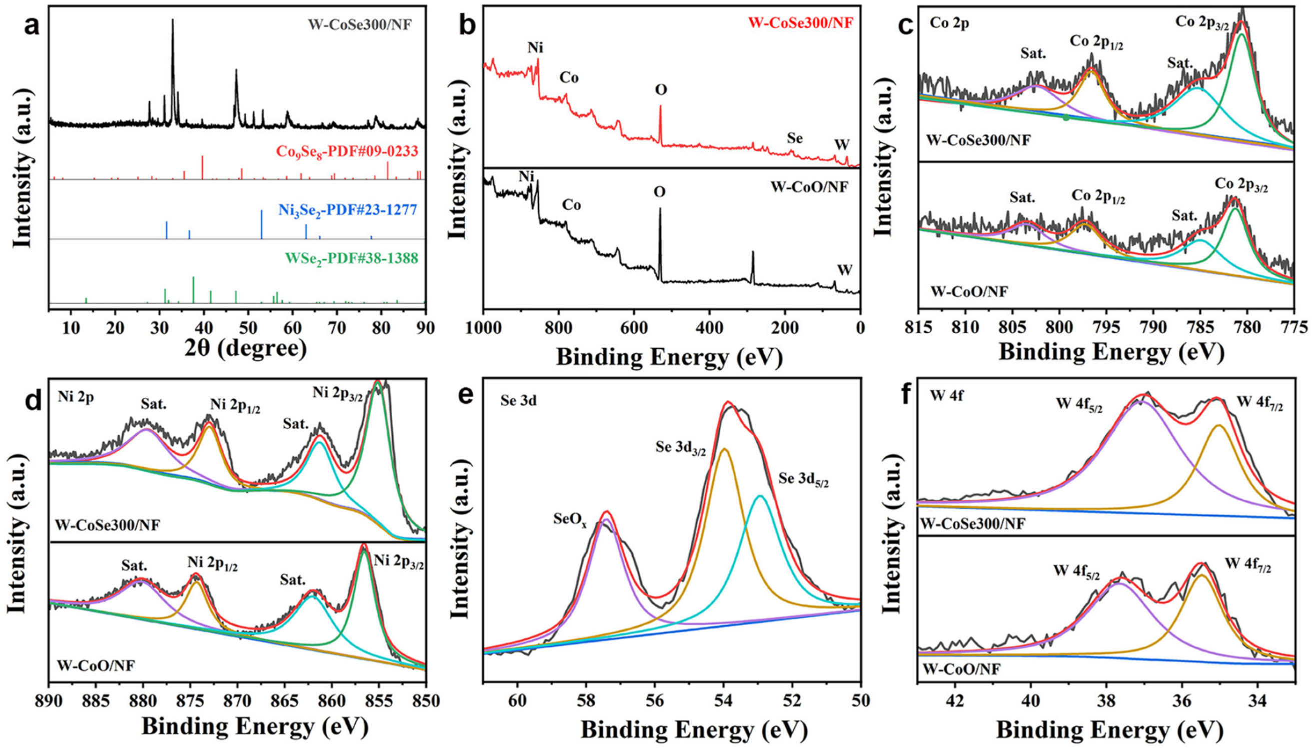

Fig. 3 (a) XRD pattern of W-CoSe300/NF. (b–f) XPS spectra of W-CoSe300/NF and W-CoO/NF: (b) survey, (c) Co 2p, (d) Ni 2p, (e) Se 3d, and (f) W 4f.

determined by linear sweep voltammetry (LSV), as shown in Fig. 4a and b. It can be found that W-CoSe300/NF possesses an optimal overpotential of 84 mV at a current density of 50 mA cm^{-2}, which is visibly better than those of W-CoO/NF (106 mV), W-CoSe200/NF (234 mV), W-CoSe400/NF (246 mV), NF (427 mV) and Pt/C (85 mV). Similarly, the W-CoSe300/NF electrocatalyst still shows the best HER performance at 100 mA cm^{-2}. In addition, the HER activity of the W-CoSe300/NF electrocatalyst prepared in this study is superior to most recently reported electrocatalysts (Table S1†). As illustrated in Fig. 4c, the Tafel slope value of W-CoSe300/NF is 97 mV dec^{-1}, which is lower than those of W-CoO/NF (123 mV dec^{-1}), W-CoSe200/NF (123 mV dec^{-1}) and W-CoSe400/NF (140 mV dec^{-1}). It can be observed from the electrochemical impedance spectroscopy (EIS) Nyquist diagram that the charge transfer resistance of the W-CoSe300/NF catalyst is small, indicating its strong charge transport ability (Fig. 4d). The electrochemically active surface area (ECSA) of the electrocatalyst is also a crucial parameter to evaluate the catalytic activity, and the values of the ECSA can be indirectly reflected by its double-layer capacitance (C_{dl}) value.[49–51] The C_{dl} values of each electrocatalyst can be obtained by cyclic voltammetry (CV) tests at different scan rates (from 20 to 100 mV s^{-1}), as depicted in Fig. S7.† Through data calculation and fitting, the C_{dl} values of different electrocatalysts can be observed in Fig. 4e. Among them, the W-CoSe300/NF electrocatalyst exhibits a maximum C_{dl} value of 24.96 mF cm^{-2}, which is greater than those of W-CoO/NF (15.92 mF cm^{-2}), W-CoSe200/NF (2.09 mF cm^{-2}) and W-CoSe400/NF (1.45 mF cm^{-2}). The remarkable C_{dl} value of W-CoSe300/NF indicates that the catalyst constructed under appropriate reaction conditions and selenide reference conditions has more active sites and higher charge transfer rates. To investigate the effect of W-doping on the intrinsic activity, the turnover frequency (TOF) of a series of W-CoSe300/NF electrocatalysts with different M ($H_3PW_{12}O_{40}$)/M ($C_4H_6CoO_4$) ratios was tested. As shown in Fig. S8,† with a ratio of 0.072, the W-CoSe300/NF electrocatalyst exhibited the highest TOF value at any potential, indicating that moderate tungsten doping can effectively enhance the intrinsic activity of the electrocatalyst. At the same time, the comparison of the specific activity of the electrocatalysts prepared at different temperatures further confirmed the excellent intrinsic activity of the W-CoSe300/NF electrocatalyst (Fig. S9†). To meet the requirements of industrial applications, electrochemical stability is also an important factor for electrocatalysts. Due to the close contact between the NF substrate and the electrocatalyst, the W-CoSe300/NF electrocatalyst shows satisfactory stability in the HER process. The electrochemical stability of W-CoSe300/NF was tested by the constant potential method and cyclic voltammetry. As described in Fig. 4f, after 5000 CV tests, the LSV curve of W-CoSe300/NF still almost coincides with that before the test, indicating its excellent HER activity and stability. Furthermore, it can be observed from the inset of Fig. 4f that the current density does not attenuate significantly during the 48 h potentiostatic method test, which further suggests the outstanding durability of W-CoSe300/NF under alkaline conditions.

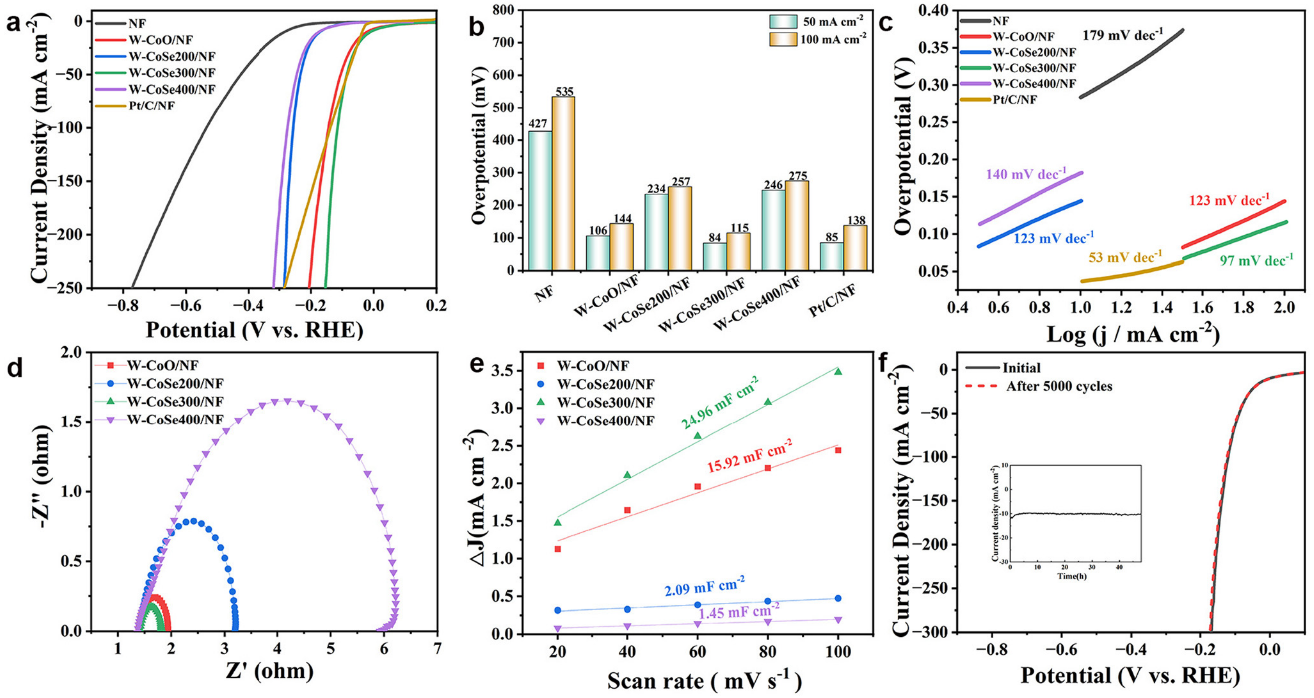

Fig. 4 HER performance: (a) LSV curves, (b) the corresponding overpotential at a current density of 50 mA cm^{-2} (η_{50}) and 100 mA cm^{-2} (η_{100}), (c) Tafel plots, (d) EIS Nyquist diagram, (e) C_{dl} values of different electrocatalysts, and (f) electrochemical stability tests of W-CoSe300/NF.

The OER performance measurements of W-CoSe300/NF and other comparable electrocatalysts were also carried out in a three-electrode system. Fig. 5a displays the LSV curves for NF, W-CoO/NF, W-CoSe200/NF, W-CoSe300/NF, W-CoSe400/NF and RuO_2/NF electrocatalysts. The bar chart in Fig. 5b further visually shows the overpotentials of different catalysts. It can be found that the η_{50} and η_{100} of the W-CoSe300/NF electrocatalyst are 283 mV and 315 mV, respectively, which are obviously superior to those of NF (556 mV, 698 mV), W-CoO/NF (404 mV, 436 mV), W-CoSe200/NF (315 mV, 338 mV), W-CoSe400/NF (397 mV, 468 mV), and RuO_2/NF (452 mV, 530 mV), indicating its superior OER activity. In the meantime, the OER performance of the W-CoSe300/NF electrocatalyst prepared in this study is much better than that of most recently reported materials (Table S2†). Moreover, the calculation results of the Tafel slope show that the slope value of W-CoSe300/NF is 34 mV dec^{-1}, which is much lower than those of NF (169 mV dec^{-1}), W-CoO/NF (149 mV dec^{-1}), W-CoSe200/NF (82 mV dec^{-1}), W-CoSe400/NF (154 mV dec^{-1}), and RuO_2 (132 mV dec^{-1}), further revealing its excellent OER kinetics (Fig. 5c). Meanwhile, the EIS Nyquist diagram shown in Fig. 5d displays that W-CoSe300/NF exhibits the smallest semicircular diameter among the four electrocatalysts, which indicates that it has suitable charge transfer resistance, further verifying the significant OER kinetics of W-CoSe300/NF. The CV curves at different scan rates were measured in the non-Faraday voltage range, and the C_{dl} values of each electrocatalyst were calculated, as illustrated in Fig. S10† and Fig. 5e. The results reveal that W-CoSe300/NF has the largest C_{dl} value of 10.16 mF cm^{-2}, which is higher than W-CoO/NF (2.24 mF cm^{-2}), W-CoSe200/NF (2.99 mF cm^{-2}) and W-CoSe400/NF (1.24 mF cm^{-2}), indirectly suggesting that it has the largest ECSA. Notably, the higher ECSA value of the electrocatalyst usually means that more active sites can be exposed to participate in the reaction during the water decomposition process, thus promoting the OER kinetics.[52–54] The OER durability of W-CoSe300/NF was also evaluated by chronoamperometry and cyclic voltammetry. As described in Fig. 5f, after 5000 CV cycles, the polarization curve of W-CoSe300/NF did not deviate significantly compared with that before the test, which confirmed its significant OER activity and stability. Moreover, the chronoamperometry curve shows that the current density does not decline obviously during the 48 hours, which further confirms the desired OER stability of W-CoSe300/NF (inset of Fig. 5f). Additionally, the comparison of the electrochemical performance of the W-CoSe300/NF catalyst loaded on different conductive substrates also corroborated the rationale for using nickel foam substrates in this study (Fig. S11–S13†).

After 120 hours of OER stability testing, the microstructure and surface elemental chemical states of the electrocatalyst were further investigated using SEM, TEM, and XPS techniques. As shown in Fig. S14a,† the SEM image of W-CoSe300/NF after testing displayed a snowflake-like structure similar to that before testing. Additionally, the TEM image shown in Fig. S14b† further confirmed this result, displaying a layered structure. Analysis of the Co 2p XPS spectrum of W-CoSe300/NF in Fig. S14c† reveals a slight increase in the peak area ratio of Co^{3+}/Co^{2+} after OER testing, possibly indicating the presence of high-valence CoOOH, a species known to promote the OER process.[55] The W 4f XPS spectrum in Fig. S14d† shows no

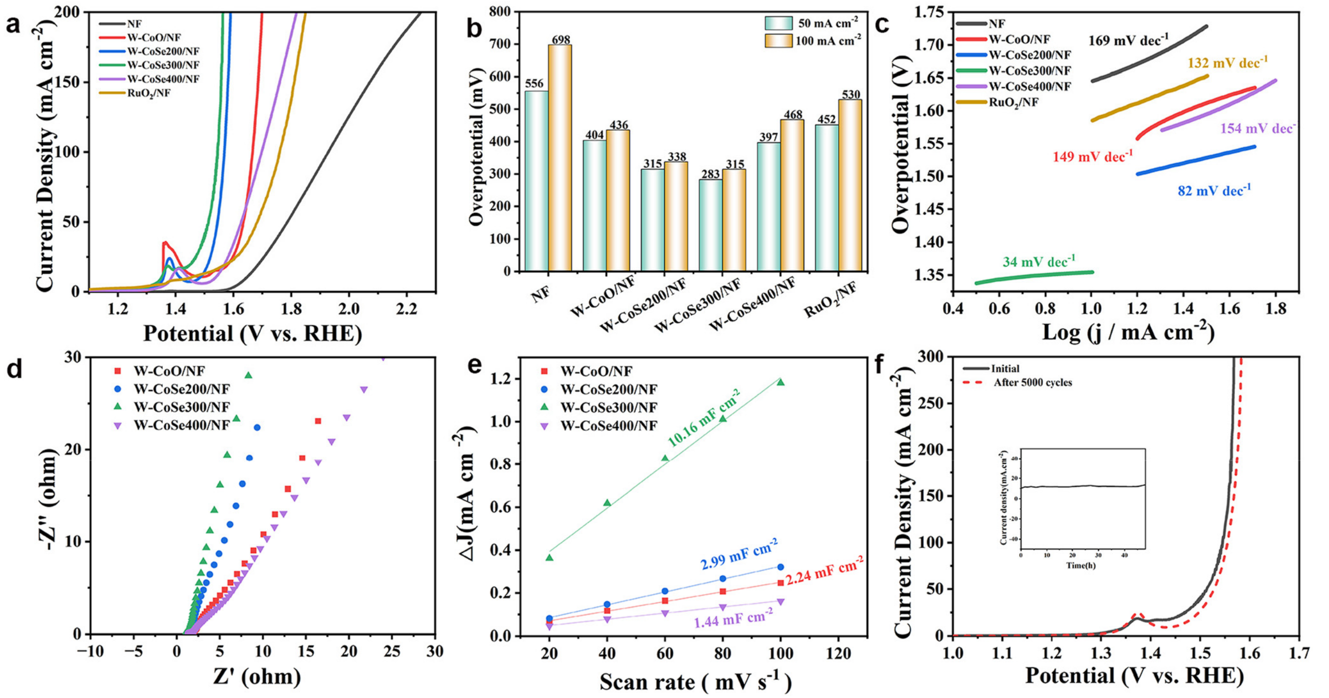

Fig. 5 OER performance: (a) LSV curves, (b) the values of η_{50} and η_{100}, (c) Tafel plots, (d) EIS Nyquist diagram, (e) C_{dl} values of different electrocatalysts, and (f) electrochemical stability tests of W-CoSe300/NF.

change in the species composition compared to before OER testing, with only a positive shift in binding energy, likely due to the strong oxidation effect at the anode increasing the electron cloud density of the W atoms, making them more stable and less reactive. Based on the post-characterization analysis, the following conclusions are obtained: during continuous OER processes, the less electronegative Se anions effectively promoted the contact between Co^{2+} and oxygen-containing species in the electrolyte, leading to the conversion of some Co^{2+} in W-CoSe300/NF into highly active CoOOH, accelerating the reaction. Simultaneously, the W atoms with high electron cloud density facilitated the timely repair of chemical bonds that fractured within the catalyst, allowing W-CoSe300/NF to maintain its original microstructure to the maximum extent.

In view of the excellent HER/OER dual functional characteristics exhibited by W-CoSe300/NF, its use as both the anode and cathode in the electrolytic tank is expected to show suitable overall water splitting (OWS) performance. As demonstrated in Fig. 6a, the W-CoSe300/NF||W-CoSe300/NF couple exhibits outstanding OWS activity, achieving a current density of 10 mA cm^{-2} at an electrolytic potential of only 1.54 V, which is significantly superior to NF||NF (1.83 V). Meanwhile, the OWS activity of the W-CoSe300/NF electrocatalyst prepared in this study is much better than that of most recently reported materials (Table S3†). Furthermore, the W-CoSe300/NF||W-CoSe300/NF system exhibits exceptional long-term stability as it can consistently operate at 10 mA cm^{-2} for a duration of 120 hours without any noticeable decline in current density (Fig. 6b).

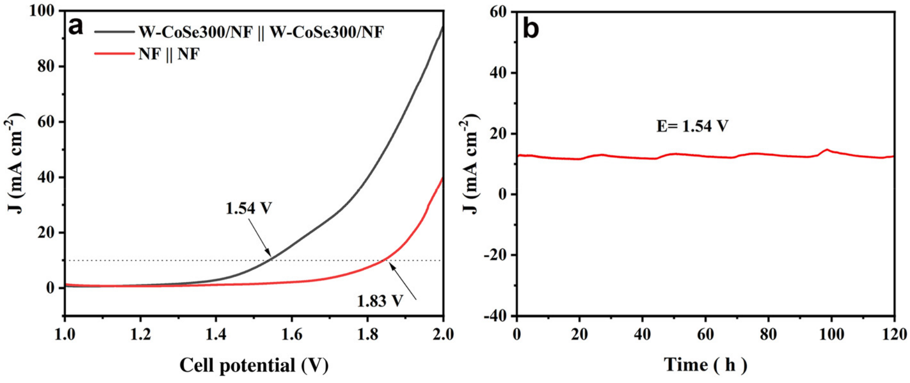

Fig. 6 OWS performance: (a) LSV curves of W-CoSe300/NF and NF. (b) Electrochemical stability tests of W-CoSe300/NF.

3. Conclusion

In summary, we prepared a W-CoSe300/NF electrocatalyst with a snowflake-like structure by hydrothermal–high temperature selenization. Due to the formation of integration defects, distortions, doping of heteroatoms and phase transitions in transition metal selenides (TMSe), their electrocatalytic performance was greatly improved. The results of electrochemical measurements reveal that the W-CoSe300/NF electrocatalyst exhibits outstanding HER/OER activity, and the overpotentials of the HER and OER at a current density of 50 mA cm^{-2} are 84 mV and 283 mV, respectively. More importantly, by using W-CoSe300/NF as both the anode and cathode for overall water splitting, a current density of 10 mA cm^{-2} can be obtained with only 1.54 V cell potential, and it can be continuously operated in this state for more than 120 h. The results show that the catalyst activity of transition metal selenides can be significantly improved by integrating suitable dopants into them. This work proposes a new pathway to construct inexpensive and efficient transition metal-based electrocatalysts.

Author contributions

Enze Fan: data curation, methodology, formal analysis, validation, and writing – original draft. Shuangqi Zhou: methodology, conceptualization, investigation, visualization, and writing – review & editing. Hanwei Zhao, Jianxin Ran, and Zhuanfang Zhang: methodology, data curation, and visualization. Guohua Dong, Yu Zang, and Wenzhi Zhang: supervision and funding acquisition. Ming Zhao, Xiaoming Huang, and Dong-Feng Chai: supervision, data curation, visualization, conceptualization, and funding acquisition.

Conflicts of interest

There are no conflicts to declare.

Acknowledgements

This research has received funding from a variety of sources, including the National Natural Science Foundation of China (Grant No. 21776144 and 5217302), the Outstanding Youth Project of the Natural Science Foundation in Heilongjiang Province (YQ2021B011), and the Fundamental Research Fund of Heilongjiang Provincial University (No. 145309622).

References

1 Y. Chang, P. Zhai, J. Hou, J. Zhao and J. Gao, *Adv. Energy Mater.*, 2022, **12**, 2102359.
2 Y. Feng, Z. Li, C.-Q. Cheng, W.-J. Kang, J. Mao, G.-R. Shen, J. Yang, C.-K. Dong, H. Liu and X.-W. Du, *Appl. Catal., B*, 2021, **299**, 120658.
3 X. Li, Q. Hu, H. Wang, M. Chen, X. Hao, Y. Ma, J. Liu, K. Tang, A. Abudula and G. Guan, *Appl. Catal., B*, 2021, **292**, 120172.
4 R. Dang, X.-F. Xu and M.-M. Xie, *J. Cent. South Univ.*, 2022, **29**, 3870–3883.
5 Y. Luo, M. Gong, J. Wang, P. Zhao, X. Yang, S. Cui, Z. Li, Z. Jiao and L. Cheng, *Colloids Surf., A*, 2022, **655**, 130119.
6 S. Zhou, X. Chen, T. Li, Y. Wei, R. Sun, S. Han and J. Jiang, *Fuel*, 2024, **357**, 129732.
7 Y. Wang, Y. Yang, X. Wang, P. Li, H. Shao, T. Li, H. Liu, Q. Zheng, J. Hu, L. Duan, C. Hu and J. Liu, *Nanoscale Adv.*, 2020, **2**, 792–797.
8 X. Huang, R. Lu, Y. Cen, D. Wang, S. Jin, W. Chen, I. Geoffrey, N. Waterhouse, Z. Wang, S. Tian and X. Sun, *Nano Res.*, 2023, **16**, 9073–9080.
9 Z. Zhang, J. Ran, Z. Wu and B. Zhao, *J. Cluster Sci.*, 2023, **34**, 1475–1482.
10 A. Ali, P. Chen, Q. U. Khan and P. K. Shen, *Int. J. Hydrogen Energy*, 2022, **47**, 15969–15981.
11 Z. Zhang, J. Ran, E. Fan, S. Zhou, D.-F. Chai, W. Zhang, M. Zhao and G. Dong, *J. Alloys Compd.*, 2023, **968**, 172169.
12 H. Feng, D. Guo, D.-F. Chai, W. Zhang, Z. Zhang, L. Bai, J. Xing and G. Dong, *Int. J. Hydrogen Energy*, 2024, **51**, 732–741.
13 Z. Kou, T. Wang, Q. Gu, M. Xiong, L. Zheng, X. Li, Z. Pan, H. Chen, F. Verpoort, A. K. Cheetham, S. Mu and J. Wang, *Adv. Energy Mater.*, 2019, **9**, 1803768.
14 X. Ding, R. Jiang, J. Wu, M. Xing, Z. Qiao, X. Zeng, S. Wang and D. Cao, *Adv. Funct. Mater.*, 2023, **33**, 2306786.
15 H. Feng, Y. Wang, D. Guo, D.-F. Chai, W. Zhang, Z. Zhang and G. Dong, *J. Alloys Compd.*, 2024, **976**, 173092.
16 M. Bai, T. Ai, W. Bao, J. Han, J. Zhang, Q. Yu, J. Liu, X. Wei, X. Zou and L. Feng, *J. Mater. Sci. Technol.*, 2024, **187**, 63–71.
17 X. Lei, X. Xie, K. Sun, S. Liu, T. Hou, H. Peng and G. Ma, *Electrochim. Acta*, 2023, **445**, 142049.
18 T. Salehi Panah, M. Shirvani and S. S. H. Davarani, *J. Alloys Compd.*, 2024, **978**, 173496.
19 B. Fang, L. Daniel, A. Bonakdarpour and D. P. Wilkinson, *Adv. Mater. Interfaces*, 2022, **9**, 2200349.
20 P. Mondal, J. Satra, D. N. Srivastava, G. R. Bhadu and B. Adhikary, *ACS Catal.*, 2021, **11**, 3687–3703.
21 W. Zhang, X. Liu, T. Liu, T. Chen, X. Shen, T. Ding, L. Cao, L. Wang, Q. Luo and T. Yao, *J. Phys. Chem. C*, 2021, **125**, 6229–6236.
22 Y.-W. Dong, X.-Y. Zhang, J.-C. Zhou, F.-L. Wang, R.-N. Luan, X. Liu, B. Liu, Y.-M. Chai and B. Dong, *Int. J. Hydrogen Energy*, 2022, **47**, 31656–31664.
23 C. Liu, Y. Hu, F. Liu, H. Liu, X. Xu, Y. Xue, J. Zhang, Y. Li and C. Tang, *Int. J. Hydrogen Energy*, 2021, **46**, 17133–17142.
24 L. Sun, M. Feng, Y. Peng, X. Zhao, Y. Shao, X. Yue and S. Huang, *J. Mater. Chem. A*, 2024, **12**, 8796–8804.
25 J.-S. Zeng, Z.-X. Qian, Q.-N. Zheng, J.-H. Tian, H. Zhang and J.-F. Li, *ChemCatChem*, 2024, **16**, e202301222.
26 L. Wu, Q. Liang, J. Zhao, J. Zhu, H. Jia, W. Zhang, P. Cai and W. Luo, *Chin. J. Catal.*, 2023, **55**, 182–190.

27 Y. Wang, X. Li, M. Zhang, J. Zhang, Z. Chen, X. Zheng, Z. Tian, N. Zhao, X. Han, K. Zaghib, Y. Wang, Y. Deng and W. Hu, *Adv. Mater.*, 2022, **34**, 2107053.

28 Q. Ding, W. Zheng, A. Zhao, Y. Zhao, K. Chen, X. Zhou, H. Zhang, Q. Li, X. Ai, H. Yang, Y. Fang and Y. Cao, *Adv. Energy Mater.*, 2023, **13**, 2203802.

29 J. Jiang, H. Su, S. Song, W. Liu, N. Li, Y. Gao and L. Ge, *Nano Res.*, 2023, **16**, 12116–12125.

30 S. L. Fereja, P. Li, J. Guo, Z. Fang, Z. Zhang, Z. Zhuang, X. Zhang, K. Liu and W. Chen, *ACS Appl. Nano Mater.*, 2021, **4**, 5992–6001.

31 L. Ding, K. Li, Z. Xie, G. Yang, S. Yu, W. Wang, H. Yu, J. Baxter, H. M. Meyer, D. A. Cullen and F.-Y. Zhang, *ACS Appl. Mater. Interfaces*, 2021, **13**, 20070–20080.

32 T. Chen and Y. Tan, *Nano Res.*, 2018, **11**, 1331–1344.

33 R. Andaveh, A. Sabour Rouhaghdam, J. Ai, M. Maleki, K. Wang, A. Seif, G. Barati Darband and J. Li, *Appl. Catal., B*, 2023, **325**, 122355.

34 Z. Pan, D. Wang, D. Zhang, Y. Yang, H. Yu, T. Wang and X. Dong, *Sens. Actuators, B*, 2024, **405**, 135378.

35 L. Yu, T. Zhou, S. Cao, X. Tai, L. Liu and Y. Wang, *Nano Res.*, 2021, **14**, 2659–2665.

36 J. Zhang, Y. Fang, Y. Chen, X. Zhang, H. Xiao, M. Zhao, C. Zhao, X. Ma, T. Hu, E. Luo, J. Jia and H. Wu, *J. Colloid Interface Sci.*, 2024, **653**, 821–832.

37 Y. Xu, R. Wang, J. Wang, Y. Zhang and T. Jiao, *J. Energy Chem.*, 2022, **71**, 36–44.

38 H. Feng, Y. Han, Y. Wang, D.-F. Chai, J. Ran, W. Zhang, Z. Zhang, G. Dong, M. Qi and D. Guo, *J. Colloid Interface Sci.*, 2024, **667**, 237–248.

39 H. Zhang, S. Wang, M. Wang, G. Li, L. Yu, X. Liu, Z. Wang and C. Zhang, *J. Rare Earths*, 2023, **41**, 870–880.

40 J. Wang, H. Xuan, L. Meng, X. Liang, Y. Li, J. Yang and P. Han, *Int. J. Hydrogen Energy*, 2023, **48**, 8144–8155.

41 Z. Cen, F. Yang, J. Wan and K. Xu, *Chem. Commun.*, 2023, **59**, 8708–8710.

42 X. Li, M. Wang, J. Fu, F. Lu, Z. Li and G. Wang, *Small*, 2023, 2310040.

43 M. Zhu, Q. Yan, Y. Xue, Y. Yan, K. Zhu, K. Ye, J. Yan, D. Cao, H. Xie and G. Wang, *ACS Sustainable Chem. Eng.*, 2022, **10**, 279–287.

44 M. Zhu, X. Bai, Q. Yan, Y. Yan, K. Zhu, K. Ye, J. Yan, D. Cao, X. Huang and G. Wang, *J. Colloid Interface Sci.*, 2021, **602**, 384–393.

45 X. Wang, Y. Zheng, J. Yuan, J. Shen, J. Hu, A.-J. Wang, L. Wu and L. Niu, *Electrochim. Acta*, 2017, **225**, 503–513.

46 T. Li, L. Ye and K. Xie, *Int. J. Hydrogen Energy*, 2024, **58**, 822–828.

47 Z. Ren, X. Ren, L. Zhang, C. Fu, X. Li, Y. Zhang, B. Gao, L. Yang, P. K. Chu and K. Huo, *ChemElectroChem*, 2019, **6**, 5229–5236.

48 T. Kavinkumar, H. Yang, A. T. Sivagurunathan, H. Jeong, J. W. Han and D.-H. Kim, *Small*, 2023, **19**, 2300963.

49 J. Ran, Z. Zhang, H. Feng, H. Zhao, D.-F. Chai, X. Huang, W. Zhang, M. Zhao, G. Dong, Y. Zang and S. Li, *Int. J. Hydrogen Energy*, 2024, **64**, 935–946.

50 X. Zhang, A. Wu, D. Wang, Y. Jiao, H. Yan, C. Jin, Y. Xie and C. Tian, *Appl. Catal., B*, 2023, **328**, 122474.

51 B. Wang, X. Chen, Y. He, Q. Liu, X. Zhang, Z. Luo, J. V. Kennedy, J. Li, D. Qian, J. Liu and G. I. N. Waterhouse, *Appl. Catal., B*, 2024, **346**, 123741.

52 I. Ahmed, V. Burman, R. Biswas, A. Roy, R. Sharma and K. K. Haldar, *New J. Chem.*, 2023, **47**, 17284–17292.

53 S.-J. Huang, S. Balu, N. R. Barveen and R. Sankar, *Colloids Surf., A*, 2022, **654**, 130024.

54 X. Han, Z. Lin, X. He, L. Cui and D. Lu, *Int. J. Hydrogen Energy*, 2020, **45**, 26989–26999.

55 N. Yao, G. Wang, H. Jia, J. Yin, H. Cong, S. Chen and W. Luo, *Angew. Chem., Int. Ed.*, 2022, **61**, e202117178.